



E^2 and gamma distributions in polygonal networksRan Li ¹, Consuelo Ibar,² Zhenru Zhou,² Seyedsajad Moazzeni,¹ Andrew N. Norris,¹ Kenneth D. Irvine ^{2,*},
Liping Liu,^{1,3,†} and Hao Lin^{1,‡}¹*Department of Mechanical and Aerospace Engineering, Rutgers,**The State University of New Jersey, New Brunswick, New Jersey 08901, USA*²*Waksman Institute and Department of Molecular Biology and Biochemistry, Rutgers,**The State University of New Jersey, New Brunswick, New Jersey 08901, USA*³*Department of Mathematics, Rutgers, The State University of New Jersey, New Brunswick, New Jersey 08901, USA*

(Received 12 December 2020; accepted 22 July 2021; published 5 October 2021)

From solar supergranulation to salt flats in Bolivia, from veins on leaves to cells on *Drosophila* wing disks, polygon-based networks exhibit great complexities, yet similarities and consistent patterns emerge. Based on analysis of 99 polygonal tessellations with a wide variety of physical origins, this work demonstrates the ubiquity of an exponential distribution in the squared norm of the deformation tensor E^2 , which directly leads to the ubiquitous presence of gamma distributions in the polygon aspect ratio, as recently demonstrated by Atia *et al.* [*Nat. Phys.* **14**, 613 (2018)]. In turn an analytical approach is developed to illustrate its origin. E^2 relates to most energy forms, and its Boltzmann-like feature allows the definition of a pseudotemperature that promises utility in a thermodynamic ensemble framework.

DOI: [10.1103/PhysRevResearch.3.L042001](https://doi.org/10.1103/PhysRevResearch.3.L042001)**I. INTRODUCTION**

Polygonal networks are one of nature's favorite ways of self-organizing, from supergranulation on the solar surface [1] to cracked dry earth [2], from ice wedges in northern Canada [3] to the scenic Salar de Uyuni in Bolivia [4], and from veins on leaves [5] to cells on *Drosophila* wing disks [6] (Fig. 1). These systems are driven by distinctive physical mechanisms, yet they share common features. Individual constituents, namely, “cells” appear to “randomize” into statistical distributions and interact with only their immediate neighbors. On the collective level, especially in dynamic and active systems, rich phenomena are observed, including unjamming and jamming, fluid-to-solid phase transitions, and flow and migration [7–15].

Despite the complexity and variabilities involved in these phenomena, similarity patterns emerge. One particularly interesting instance was provided recently by Atia *et al.* [16]. Within the context of confluent biological tissue and based on extensive experiments both *in vitro* and *in vivo*, the authors found that data on cell aspect ratio collapse and follow a normalized gamma distribution, implying a universal principle governing the geometric configuration and pertinent processes.

What is the basis of this universality? Does it carry beyond the biological context? This Letter comprises of a two-part

discovery to answer these questions. In the first part, we demonstrate that the gamma distribution in the polygon aspect ratio derives from an exponential distribution in the squared strain tensor norm E^2 . We show that such gamma distributions do not share a physical origin similar to those in the granular packing system as suggested by Atia *et al.* [16,17], but rather are an approximation of a unifying solution that we develop. More importantly, we are able to extend the universality of the observations to a wide variety of systems (99 data sets in 8 groups) that include convection patterns (solar supergranulation), landforms (in salt flats, on Mars, and in or near the Arctic), cracked dry earth, and biological patterns (veins on leaves, cells on *Drosophila* wing disks, and plated Madin-Darby Canine Kidney cells (MDCK); Fig. 1 and Table I). Both exponential and gamma distributions persist in all data examined. In the second part, we tackle the origin of the E^2 distribution and present a theoretical framework to accurately compute E^2 from vertex statistics. Importantly, E^2 is closely related to common definitions of system energy, including all of the bulk-, perimeter-, and moment-based (known as the quantizer) forms [7,10,18–21]. The Boltzmann-like feature of E^2 enables the definition of a pseudotemperature which promises utility in an ensemble-based thermodynamic framework [22–25].

II. E^2 AND ITS RELATIONSHIP WITH THE ASPECT RATIO

In this part, we define E^2 and analytically establish its relationship with the polygon aspect ratio. We demonstrate that a k -gamma distribution in the latter is derivable from an exponential distribution in the former. We begin by defining the mean-field deformation tensor \mathbf{E} . An exemplary processed image of a *Drosophila* wing disk 120 h after egg laying is shown in Fig. 1(h), where the color scale indicates the

*Corresponding author: irvine@waksman.rutgers.edu†Corresponding author: liu.liping@rutgers.edu‡Corresponding author: hlin@soe.rutgers.edu

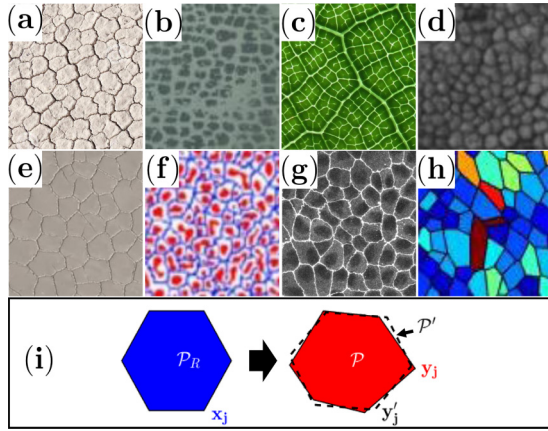


FIG. 1. (a)–(h) Examples of randomized polygonal networks. (a) Land cracks due to desiccation [2]. (b) Ice wedges from northern Canada [3]. (c) Veins on a *Ficus lyrata* leaf [5]. (d) Desiccation pattern of an ancient lake on Mars (HiRISE image: PSP_002140_2025 [26], credit to NASA/JPL/University of Arizona). (e) A snapshot of Salar de Uyuni in Bolivia, the world’s largest salt flat [4]. (f) Supergranulation on the solar surface [1]. (g) Plated MDCK cells. (h) A processed image of a developing *Drosophila* wing disk with the aspect ratio of cells color mapped. (i) A regular hexagon \mathcal{P}_R (blue, with vertices \mathbf{x}_j), a deformed hexagon \mathcal{P} (red, \mathbf{y}_j), and a uniform deformation approximation \mathcal{P}' (black dashed outline, \mathbf{y}'_j).

magnitude of the cell aspect ratio. We choose as our reference frame a regular n -polygon centered at the origin, with vertices

$$\mathbf{x}_j = r_0 \mathbf{e}_j, \quad \mathbf{e}_j = [\cos(j2\pi/n), \sin(j2\pi/n)], \quad (1)$$

for $j = 1, \dots, n$. This polygon is denoted by \mathcal{P}_R , and r_0 is to be determined such that \mathcal{P}_R has the same area as the polygon in comparison. Figure 1(i) uses $n = 6$, a hexagon, as an illustrative example. We consequently regard any n -sided polygon \mathcal{P} with vertices \mathbf{y}_j as a “deformation” from \mathcal{P}_R , namely, $\mathbf{y}_j = \mathbf{x}_j + \mathbf{u}_j$, where we also assume that their centroids (defined by Eq. (S6) in the Supplemental Material (SM) [27]) are aligned. The deformation is, in general, nonuniform, in the sense that for vertex number $n \geq 3$, a single deformation tensor of $\mathbf{F} \in \mathbb{R}^{2 \times 2}$ cannot be identified by $\mathbf{y}_j = \mathbf{F}\mathbf{x}_j$ for all j . Nevertheless, we can introduce an affine approximation, namely, $\mathbf{y}_j \approx \mathbf{y}'_j = \mathbf{F}\mathbf{x}_j$. The use of a uniform deformation to approximate the local and nonuniform deformation field is effectively coarse graining, reducing the degree of freedom

from $2n$ to 4 and suppressing the fluctuations. This idea is illustrated in Fig. 1(i) (right), where \mathcal{P}' is the approximate and uniformly deformed polygon. From \mathbf{F} we define the usual strain tensor and its squared Frobenius norm,

$$\mathbf{E} = (\mathbf{F}^T \mathbf{F})^{\frac{1}{2}} - \mathbf{I} \approx [(\mathbf{F} - \mathbf{I}) + (\mathbf{F} - \mathbf{I})^T]/2, \quad (2)$$

where \mathbf{I} is the identity tensor and the Frobenius norm is $|\mathbf{E}|^2 = \text{Tr}(\mathbf{E}^T \mathbf{E})$. Here we will use $|\mathbf{E}|^2$ and E^2 (terminology) interchangeably. The restriction to area-conserved deformation requires that $\text{Tr} \mathbf{E} = 0$, which is satisfied by choosing r_0 in (1). Consequently, \mathbf{E} has a degree of freedom of 2. We pursue an analytical expression for \mathbf{E} by minimizing the difference between \mathbf{y}_j ’s and \mathbf{y}'_j ’s, from which we obtain [27]

$$|\mathbf{E}|^2 = \sum_{i=1}^n \sum_{j=1}^n \mathbf{v}_i \cdot \mathbf{C}_{ij} \mathbf{v}_j, \quad (3)$$

$$\mathbf{C}_{ij} = \frac{2}{n^2} [(\mathbf{e}_i \cdot \mathbf{e}_j) \mathbf{I} + \mathbf{e}_j \otimes \mathbf{e}_i - \mathbf{e}_i \otimes \mathbf{e}_j], \quad (4)$$

where $\mathbf{v}_j = \mathbf{u}_j/r_0$, $r_0 = \frac{1}{n} \sum_{j=1}^n \mathbf{y}_j \cdot \mathbf{e}_j$, and \otimes denotes a dyadic product.

Next, we show that if E^2 follows an exponential distribution (validated below via both data and analysis), namely, $\rho_E(|\mathbf{E}|^2) = \beta \exp(-\beta|\mathbf{E}|^2)$, then the aspect ratio follows a k -gamma distribution such as that shown in [16]. Here $\rho(\cdot)$ denotes a probability density function (PDF), and β is similar to an inverse temperature. The aspect ratio a_r of the polygon is calculated via the second area moment and is related to E^2 as [27]

$$a_r^2 = (x + 1)^2 = g(|\mathbf{E}|^2), \quad (5)$$

where $g(t) = 1 + 2t^2 + 4t + [(2t^2 + 4t + 1)^2 - 1]^{1/2}$ and for convenience we have defined a shape factor x . Based on (5), a transformation $\rho_E(|\mathbf{E}|^2) d|\mathbf{E}|^2 = \rho_X(x) dx$ leads to

$$\rho_X(x) = \rho_E(|\mathbf{E}|^2) \frac{d|\mathbf{E}|^2}{dx} = \beta \zeta'(x) \exp[-\beta \zeta(x)], \quad (6)$$

where $\zeta(x) = g^{-1}[(x + 1)^2]$ and the superscript denotes an inverse function. Equation (6) is our prediction of the distribution in the aspect ratio.

III. DATA VALIDATE E^2 AND a_r DISTRIBUTIONS

Both distributions and their relationship are extensively validated, with a total of 99 data sets spanning 8 groups, as

TABLE I. Summary of data for a total of $M_{\text{tot}} = 99$ tessellations. Abbreviations used in Fig. 3 are given in parentheses. M is the number of data sets in each type; N is the number of polygons in each set (a range is provided). R^2 for $|\mathbf{E}|^2$ indicates the quality of fitting (e.g., in the left column of Fig. 2); R^2 for $a_r - 1$ indicates the quality of agreement between theory and data (e.g., in the middle column of Fig. 2).

Type (abbreviation)	M	N	$R^2, \mathbf{E} ^2$	$R^2, a_r - 1$
Salt flat of Uyuni (Salt Flat)	7	193–849	0.994 ± 0.0058	0.939 ± 0.0255
Landforms on Mars (Mars)	9	219–5826	0.986 ± 0.0125	0.935 ± 0.0461
Veins on leaves (Leaves)	6	338–6050	0.994 ± 0.0047	0.936 ± 0.0328
Landforms in the Arctic (Arctic)	11	104–1061	0.982 ± 0.0169	0.902 ± 0.0728
Supergranulation on the solar surface (Solar)	9	192–1645	0.991 ± 0.0075	0.932 ± 0.0463
Cracked dry earth (Cracks)	11	298–1596	0.992 ± 0.0067	0.943 ± 0.0353
<i>Drosophila</i> wing disk (Droso)	42	902–4205	0.991 ± 0.0083	0.955 ± 0.0335
Plated MDCK cells (MDCK)	4	1148–2283	0.997 ± 0.0012	0.936 ± 0.0157

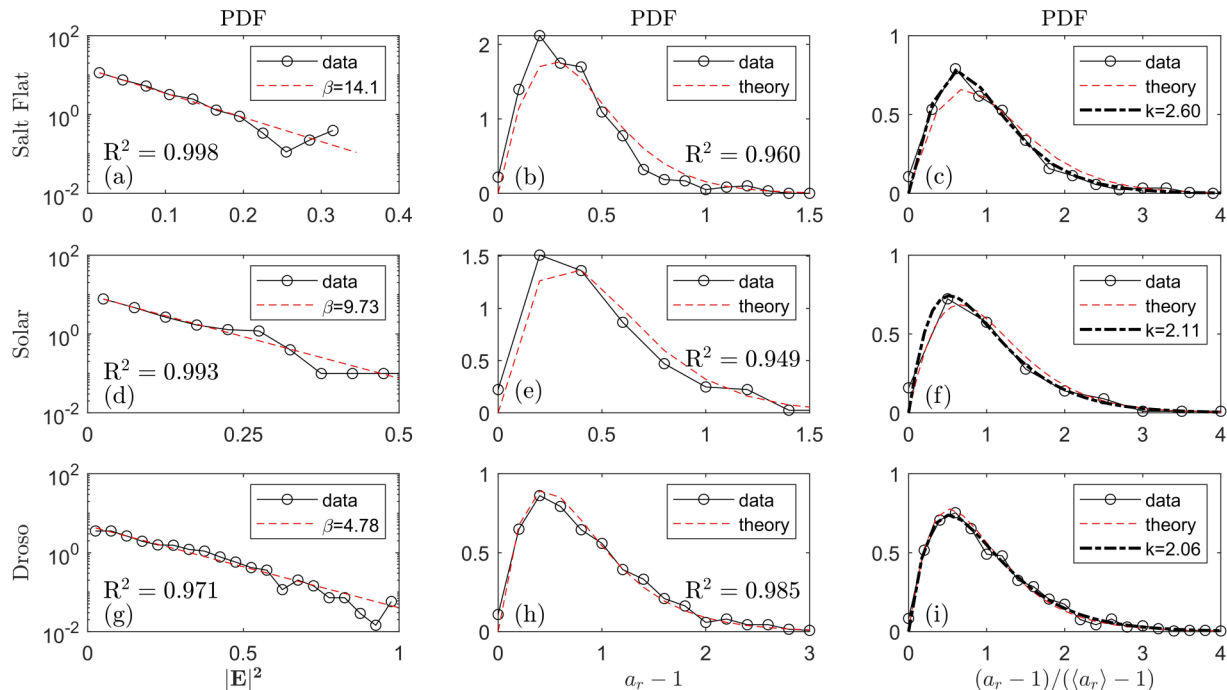


FIG. 2. Universality in strain and aspect ratio distributions. The left column shows the PDFs of $|\mathbf{E}|^2$, fitted with an exponential form $\exp(-\beta|\mathbf{E}|^2)$ to extract β . β is then used in (6) to generate the theoretical curves in the middle column (dashed lines), in comparison to the aspect ratio (symbols). The coefficients of determination R^2 are shown. In the right column both data and theoretical curves from the middle column are normalized and fitted with a k -gamma function (7) (thick dashed lines). k is extracted and shown in the legends. Data are from [28,29] and this work.

summarized in Table I; detailed descriptions, data sources, and the method of analysis are presented in the SM [27]. Figures 2 and S2 use eight representative cases from each group to demonstrate the agreement. The left column shows the PDFs of $|\mathbf{E}|^2$, which are very well fitted by the exponential form, $\exp(-\beta|\mathbf{E}|^2)$, where β is extracted as a fitting parameter. [See also Fig. 4(b) below, where all $|\mathbf{E}|^2$ profiles are presented and the value of β is theoretically predicted.]

The middle column of Fig. 2 shows the PDFs of the shape factor, $a_r - 1$ (symbols). The theoretical predictions per Eq. (6) are shown by dashed lines and exhibit excellent agreement with the data. They are generated per Eq. (6), with the single input parameter, β , extracted from the analysis of the $|\mathbf{E}|^2$ distribution.

Last, in the right column, the PDFs for $a_r - 1$ are normalized with $\langle a_r \rangle - 1$, where $\langle \cdot \rangle$ denotes a mean. Both data and theoretical predictions are normalized following this practice. The dot-dashed lines are best fits using a k -gamma distribution following [16]

$$\rho_{kG}(x_1; k) = \frac{k^k}{\Gamma(k)} x_1^{k-1} \exp(-kx_1), \quad (7)$$

where $\Gamma(k)$ is the gamma function and k is the single fitting parameter. The agreement is evident, and the k values are found to vary by about 2–3.

Overall, corroboration between theory and data is quantified by the coefficient of determination R^2 , which is listed in Table I for all cases. The values are uniformly close to 1. The validity of the theoretical prediction (6) is also attested by Fig. 3(a). Here we define a pseudotemperature T as the inverse of β , namely, $T = \beta^{-1}$. To make a comparison with

the data, a theoretical prediction is generated by using (6) to obtain the mean.

The above results validate that the E^2 does follow an exponential, Boltzmann-like distribution. The universality of this distribution in all data sets, according to our theory, necessarily leads to a universality of k -gamma distributions for the aspect ratio. That is, the validity extends beyond the confluent tissues studied in [16] to all systems we analyzed.

IV. E² DISTRIBUTION IS A χ^2 DISTRIBUTION

In this part, we demonstrate the origin of the highly regular statistical distribution in E^2 . We first show that due to the small degree of freedom of \mathbf{E} , we can write $|\mathbf{E}|^2$ as the sum of two squared entities. These entities are then shown to follow normal distributions due to the machinery of the central limit theorem. The combined effects lead to an exponential distribution for $|\mathbf{E}|^2$ as a special case of the χ^2 distribution. Figure 3(b) shows results comparing the pseudotemperature computed from data with the theoretical prediction we develop below (denoted “theory”). Here the subscript n denotes a restriction to the subensemble of n -gons, $T_n := \langle |\mathbf{E}|^2 \rangle_n$. Polygons other than $n = 4-8$ are of statistically insignificant occurrences and are not included.

The key relationship we utilize is a quadratic form to compute $|\mathbf{E}|^2$ given vertex displacement \mathbf{v}_j . We concatenate \mathbf{v}_j 's to a vector in \mathbb{R}^{2n} , namely, $\hat{\mathbf{v}} := [\mathbf{v}_1; \dots; \mathbf{v}_n] = [\hat{v}_1; \dots; \hat{v}_{2n}]$. (We similarly define other vectors and tensors from their two-dimensional counterparts and denote them with a hat.) We then have $|\mathbf{E}|^2 = \hat{\mathbf{v}} \cdot \hat{\mathbf{C}} \hat{\mathbf{v}}$, where $\hat{\mathbf{C}} \in \mathbb{R}_{\text{sym}}^{2n \times 2n}$ has block components \mathbf{C}_{ij} given in (4). $\hat{\mathbf{C}}$ has a single eigenvalue $2/n$ of

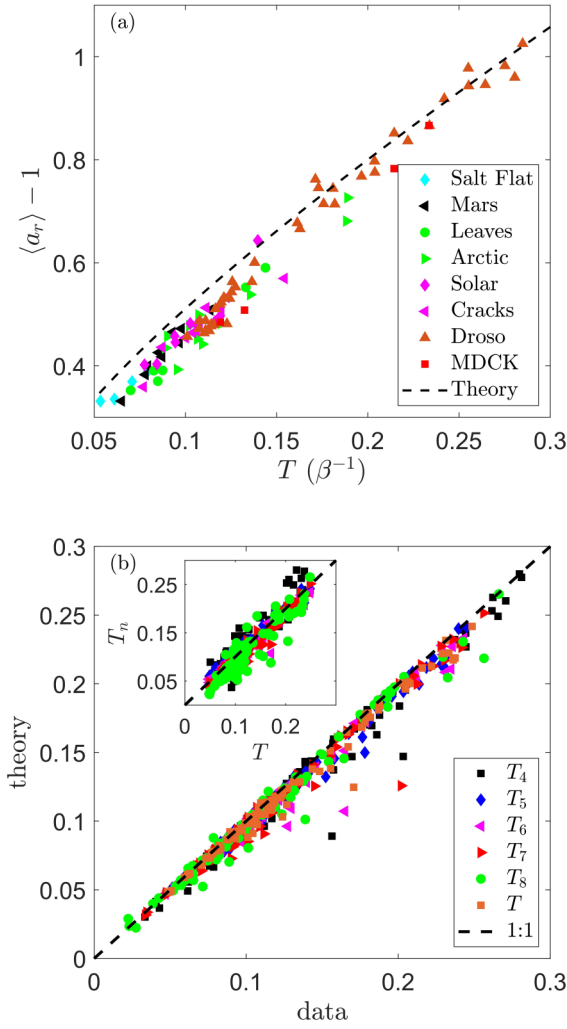


FIG. 3. (a) Overall correlation between a_r and $T(\beta^{-1})$ for all 99 data sets (symbols); the theoretical prediction (dashed line) is generated per (6). (b) A comparison between data and predicted temperature, T_n and T (“theory”). The inset shows that subensemble temperatures T_n are quantitatively similar to the tessellation temperature T .

multiplicity 2 [27]. $|\mathbf{E}|^2$ can thus be reduced to a particularly simple form,

$$|\mathbf{E}|^2 = (2/n)(\hat{w}_1^2 + \hat{w}_2^2), \quad (8)$$

where $\hat{w}_k := \hat{\mathbf{p}}_k \cdot \hat{\mathbf{v}}$ and $\hat{\mathbf{p}}_k$ is an eigenvector of $\hat{\mathbf{C}}$. If $\hat{\mathbf{v}}$ is characterized by a covariance matrix, $\hat{\Sigma}$, then the variance of \hat{w}_k is $\text{Var}(\hat{w}_k) = \hat{\mathbf{p}}_k \cdot \hat{\Sigma} \hat{\mathbf{p}}_k = \text{Tr}(\hat{\mathbf{p}}_k \otimes \hat{\mathbf{p}}_k \cdot \hat{\Sigma})$ [30], and T_n is readily computed as

$$T_n = \langle |\mathbf{E}|^2 \rangle_n = (2/n) \text{Var}(\hat{w}_1 + \hat{w}_2) = \text{Tr}(\hat{\mathbf{C}} \hat{\Sigma}). \quad (9)$$

Note that we have used $\hat{\mathbf{C}} = (2/n)(\hat{\mathbf{p}}_1 \otimes \hat{\mathbf{p}}_1 + \hat{\mathbf{p}}_2 \otimes \hat{\mathbf{p}}_2)$ and $\hat{\mathbf{v}}$ has a zero mean. Equation (9) is a precise expression to compute T_n given $\hat{\Sigma}$ and is used to generate the theoretical predictions in Fig. 3(b). The tessellation average T can be computed by taking the weighted sum of T_n , namely, $T = \sum_n (N_n T_n) / \sum_n N_n$, where N_n is the number of n -gons. On the other hand, subensemble temperatures are typically quantita-

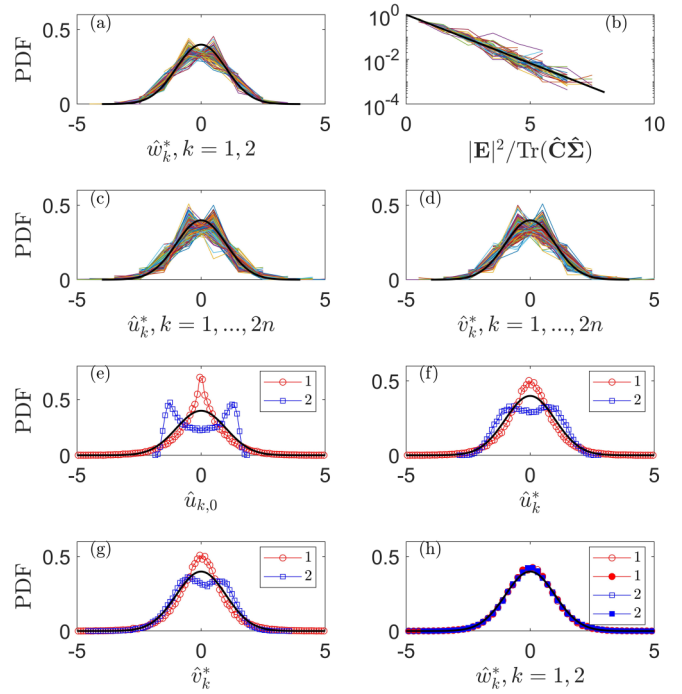


FIG. 4. Normality of key variables; an asterisk (*) denotes normalization by its own standard deviation to compare with $N(0, 1)$ (dark lines). (a) $\hat{w}_{1,2}$ for all tessellations (198 profiles). (b) Normalized $|\mathbf{E}|^2$ follows a simple exponential distribution (99 profiles). (c) and (d) The normality of \hat{u}_k and \hat{v}_k for $n = 6$, 1188 profiles each. (e) Initial displacement for two exemplary cases. (f) and (g) \hat{u}_k and \hat{v}_k asymptote toward normality. (g) Normalities of $\hat{w}_{1,2}$ are well established.

tively similar to the tessellation temperature, as shown in the inset in Fig. 3(b).

If we further assume that $\hat{w}_{1,2}$ follow identical normal distributions, immediately, we have

$$\rho_E(|\mathbf{E}|^2) = (1/T_n) \exp(-|\mathbf{E}|^2/T_n). \quad (10)$$

In other words, the exponential distribution arises actually as a χ^2 distribution with two degrees of freedom. On the other hand, if the variances $\text{Var}(\hat{w}_{1,2})$ are not identical but quantitatively similar, which is true for all tessellations we study (Fig. S5), Eq. (10) still holds to the leading order. (This point is straightforward to prove via Taylor expansion and not shown here for brevity.) Note that even in this situation, per (9) the formula for T_n is still accurate without approximation. This provides an essential illustration of the origin of the E^2 distribution, and Eq. (10) is a main result of the current work. It remains to be shown below that $\hat{w}_{1,2}$ distributions are, indeed, approximately normal and independent.

V. ASYMPTOTIC NORMALITY CONTRIBUTES TO STATISTICAL REGULARITY

Figure 4(a) presents $\hat{w}_{1,2}$ in the hexagon subensemble ($n = 6$) for all 99 tessellations, whereas the cases for $n = 5$ and 7 are included in the SM [27]. PDFs are all normalized for comparison with the standard Gaussian $N(0, 1)$ (dark solid lines). Although the PDFs exhibit appreciable fluctuations due to the relatively small sample size in the n subensemble, the

approximate normalities are evident. Quantitative similarities of $\hat{w}_{1,2}$ are demonstrated in Fig. S5. In addition, $\hat{w}_{1,2}$ are, indeed, only weakly dependent, as $\text{Cov}(\hat{w}_1, \hat{w}_2)/\text{Var}(\hat{w}_1) = 0.078 \pm 0.046$ for all cases, consistent with the anticipated two degrees of freedom. All E² distributions normalized by the predicted temperature T_n are shown in Fig. 4(b).

The apparent candidate to explain the resulting normality is the central limit theorem in the generalized version for dependent and identical random variables [31], noting that \hat{w}_k derives from \hat{v}_k via a linear combination. It is peculiar to note that \hat{u}_k and \hat{v}_k themselves also demonstrate approximate normality, shown in Figs. 4(c) and 4(d). The normality in \hat{u}_k is again explained by the central limit theorem. We can write $\hat{\mathbf{u}}$, the concatenated vector for \mathbf{u}_j 's, as $\hat{\mathbf{u}} = \hat{\mathbf{R}}(\hat{\mathbf{y}} - \langle \hat{\mathbf{y}} \rangle)$, where $\hat{\mathbf{R}} := \hat{\mathbf{I}} - \frac{1}{n} \hat{\mathbf{e}} \otimes \hat{\mathbf{e}}$ [27]. In the absence of apparent anisotropy, components of $\hat{\mathbf{y}} - \langle \hat{\mathbf{y}} \rangle$ are approximately identical, satisfying the precondition of the theorem. Hence, \hat{u}_k asymptotes to normality. On the other hand, we have $\hat{\mathbf{v}} = \hat{\mathbf{u}}/r_0$ and $r_0 = (\hat{\mathbf{y}} \cdot \hat{\mathbf{e}})/n$. The normality in $\hat{\mathbf{v}}$ is difficult to theoretically prove. However, it is reasonable to speculate that the loss of the apparent scale would create similarity to preserve or even enhance normality [see also Figs. 4(f) and 4(g)]. In addition, it is extensively confirmed by the data, as shown in Fig. 4(d).

The asymptotic normality can be better illustrated via a simple Monte Carlo simulation following the schematic in Fig. 1(i), where we temporarily restrict ourselves to an isolated hexagon, and initial (centroid-uncorrected) displacements $\hat{u}_{k,0}$ ($k = 1, 2, \dots, 2n$) are prescribed according to independent, identical distributions, as shown in Fig. 4(e) [27]. Two representative cases are examined; the first has a steeper than Gaussian initial descent (red), and the second is non-monotonic (blue). In Figs. 4(f) and 4(g), both \hat{u}_k and \hat{v}_k already demonstrate trending toward normality, although some differences from $N(0, 1)$ are still visible. Note that \hat{u}_k is obtained from $\hat{u}_{k,0}$ after centroid correction, and only an arbitrary index k is shown as these distributions are expected to be identical. Subsequently, in Fig. 4(h) the normality of $\hat{w}_{1,2}$ is well established. $|\mathbf{E}|^2$ distribution quantitatively follows our theoretical prediction and is not shown. Although only two exemplary tests are presented, repeated simulations reveal the same asymptotic trend to normality, and the quantitative relationships (9) and (10) always hold.

In summary, the above exercises demonstrate that asymptotic normality is prevalent in planar tessellations, as key variables derive from linear combinations of statistically similar components. As a result E² distributions become highly regular due to combined normality and its low dimensionality.

VI. PHYSICAL IMPLICATIONS

Atia *et al.* contemplated that the gamma distributions in aspect ratio have a physical origin similar to granular packing systems, in which the conservation of area gives rise to the k -gamma distribution, where k is the number of “local elementary cells” [17]. However, in such a theory k is typically a large number when compared with values in [16] or here. This Letter indicates that it is rather an approximation of solution (6) derived above, and k is an empirical fitting parameter which is positively related to β [Fig. S7(a)]. This trend is fully corroborated with data from our own work and Atia *et al.* [16]

(Fig. 3 therein), as well as predictions from a self-propelled Voronoi model in the supplemental information of the latter.

We propose that the deformation tensor \mathbf{E} is also a more fundamental quantity with evident physical meaning: It represents deformation and hence is typically associated with energy in one form or another. Some of the usual possibilities can be contemplated. If the energy is bulk elastic in nature, then any physically reasonable elastic model of a polygon must follow the form $\Delta\Psi = \mu|\mathbf{E}|^2$ [32], where μ is the first Lamé constant [27]. On the other hand, if energy is associated with edge lengths or perimeters, such as in the case of models for two-dimensional confluent tissues [7,10,21], the linear dependence on $|\mathbf{E}|^2$ is still a formally valid approximation to leading order [27]. Last but not least, in the quantizer problem [18–20] the cellwise energy functional is the moment of inertia, which is $\text{Tr}\mathbf{M} = 2m_0(1 + |\mathbf{E}|^2)$ in both two and three dimensions [27], and $2m_0$ is the moment of inertia of the regular reference polygon \mathcal{P}_R . Thus, its distribution can be computed by knowing both the area and E² distributions. These examples of constitutive relations cover a reasonably wide range of physical systems.

Above we have taken the liberty of naming a pseudotemperature T (or T_n for the subensembles). Indeed, such a definition is both tempting and appropriate in the presence of a Boltzmann-like distribution. The tests by Dean and Lefèvre [25] and McNamara *et al.* [23] become trivial: The ratio of two overlapping exponential distributions will necessarily give another exponential distribution. We therefore name this pseudotemperature the “E² temperature.” This temperature quantifies the overall deformation and possibly also system energy. Not surprisingly, this temperature is very well correlated with a similar pseudotemperature defined in Atia *et al.* [16] due to the direct relationship between $|\mathbf{E}|^2$ and the aspect ratio [Fig. S7(b)]. On the other hand, the relationship between the E² temperature and “compactivity” in a granular assembly such as in [22,23] awaits further exploration. In our ongoing endeavor we attempt to incorporate this temperature into an ensemble framework.

We have thus demonstrated three main points in this work: (i) An exponential distribution in E² leads to a k -gamma distribution in the aspect ratio. In fact, k -gamma distributions are mere approximations of a more basic solution that depends on the E² temperature. (ii) E² arises as a χ^2 distribution which results from both asymptotic normality and its small dimensionality, which is analogous to the small dimensionality of the volume function in granular assembly [33]. (iii) E² and aspect ratio distributions as well as normality in displacements are true universal features, as we have shown via both a large collection of data and theoretical derivations illustrating their origins. The strong regularity in E² and vertex displacements are “hidden patterns” revealed by this work. The mean-field strain tensor, with its clear physical and geometric meaning, is an ideal quantity connecting the conservation principles, the energy landscape, and the geometric distributions. Analysis may also extend to polytopes in three and higher dimensions.

ACKNOWLEDGMENTS

The authors are grateful to Dr. Y. Pan for providing fixed wing disk images in the *Drosophila* group. The authors acknowledge helpful discussions with Dr. T. Shinbrot and

funding support from NIH Grant No. R21 CA220202-02 [principal investigator (PI): H.L.]; NSF Grants No. CMMI

1351561 and No. DMS 1410273 (PI: L.L.), and NIH Grant No. R35 GM131748 (PI: K.D.I.).

- [1] J. Hirzberger, L. Gizon, S. K. Solanki, and T. L. Duvall, Structure and evolution of supergranulation from local helioseismology, in *Helioseismology, Asteroseismology and MHD Connections*, edited by L. Gizon, P. S. Cally, and J. Leibacher (Springer, New York, 2008), pp. 415–435.
- [2] Kojihirano, Dry lake bed texture, <https://www.dreamstime.com/stock-photo-dry-lake-bed-texture-crackled-earth-racetrack-death-valley-national-park-california-image41139404>.
- [3] D. Ronald, High centered orthogonal ice wedge polygons in northern Canadian archipelago, 2009, <http://permafrost.gi.alaska.edu/photos/image/80>.
- [4] Fly around the world, Online video: Travel the world, Uyuni voll, Bolivia by drone (Phantom), $t = 101$ s (2016), <https://www.youtube.com/watch?v=GSYLH462Nis>.
- [5] D. Clode, *Ficus lyrata* leaf, 2012, <https://reforestation.me/flower-photos-1/>.
- [6] Y. Pan, I. Heemskerk, C. Ibar, B. I. Shraiman, and K. D. Irvine, Differential growth triggers mechanical feedback that elevates Hippo signaling, *Proc. Natl. Acad. Sci. USA* **113**, E6974 (2016).
- [7] D. Bi, J. H. Lopez, J. M. Schwarz, and M. L. Manning, A density-independent rigidity transition in biological tissues, *Nat. Phys.* **11**, 1074 (2015).
- [8] R. Farhadifar, J. Röper, B. Aigouy, S. Eaton, and F. Jülicher, The influence of cell mechanics, cell-cell interactions, and proliferation on epithelial packing, *Curr. Biol.* **17**, 2095 (2007).
- [9] S. Garcia, E. Hannezo, J. Elgeti, J.-F. Joanny, P. Silberzan, and N. S. Gov, Physics of active jamming during collective cellular motion in a monolayer, *Proc. Natl. Acad. Sci. USA* **112**, 15314 (2015).
- [10] S. Kim and S. Hilgenfeldt, Cell shapes and patterns as quantitative indicators of tissue stress in the plant epidermis, *Soft Matter* **11**, 7270 (2015).
- [11] A. J. Liu and S. R. Nagel, Jamming is not just cool any more, *Nature (London)* **396**, 21 (1998).
- [12] K. D. Nnetu, M. Knorr, S. Pawlizak, T. Fuhs, and J. A. Kas, Slow and anomalous dynamics of an MCF-10A epithelial cell monolayer, *Soft Matter* **9**, 9335 (2013).
- [13] J.-A. Park *et al.*, Jamming and cell shape in the asthmatic airway epithelium, *Nat. Mater.* **14**, 1040 (2015).
- [14] M. Sadati, N. T. Qazvini, R. Krishnan, C. Y. Park, and J. J. Fredberg, Collective cell migration and cell jamming, *Differentiation* **86**, 121 (2013).
- [15] V. Trappe, V. Prasad, L. Cipelletti, P. N. Segre, and D. A. Weitz, Jamming phase diagram for attractive particles, *Nature (London)* **411**, 772 (2001).
- [16] L. Atia, D. Bi, Y. Sharma, J. A. Mitchel, B. Gweon, S. A. Koehler, S. J. DeCamp, B. Lan, J. H. Kim, R. Hirsch, A. F. Pegoraro, K. H. Lee, J. R. Starr, D. A. Weitz, A. C. Martin, J.-A. Park, J. P. Butler, and J. J. Fredberg, Geometrical constraints during epithelial jamming, *Nat. Phys.* **14**, 613 (2018).
- [17] T. Aste and T. DiMatteo, Emergence of Gamma distributions in granular materials and packing models, *Phys. Rev. E* **77**, 021309 (2008).
- [18] Q. Du and D. Wang, The optimal centroidal Voronoi tessellations and the Gershgorin's conjecture in the three-dimensional space, *Comput. Math. Appl.* **49**, 1355 (2005).
- [19] T. M. Hain, M. A. Klatt, and G. E. Schröder-Turk, Low-temperature statistical mechanics of the QuantaTizer problem: Fast quenching and equilibrium cooling of the three-dimensional Voronoi liquid, *J. Chem. Phys.* **153**, 234505 (2020).
- [20] M. A. Klatt, J. Lovrić, D. Chen, S. C. Kapfer, F. M. Schaller, P. W. A. Schönhofer, B. S. Gardiner, A.-S. Smith, G. E. Schröder-Turk, and S. Torquato, Universal hidden order in amorphous cellular geometries, *Nat. Commun.* **10**, 811 (2019).
- [21] M. L. Manning, R. A. Foty, M. S. Steinberg, and E.-M. Schoetz, Coaction of intercellular adhesion and cortical tension specifies tissue surface tension, *Proc. Natl. Acad. Sci. USA* **107**, 12517 (2010).
- [22] S. F. Edwards and D. V. Grinev, Statistical mechanics of vibration-induced compaction of powders, *Phys. Rev. E* **58**, 4758 (1998).
- [23] S. McNamara, P. Richard, S. K. de Richter, G. LeCaër, and R. Delannay, Measurement of granular entropy, *Phys. Rev. E* **80**, 031301 (2009).
- [24] S. Henkes, C. S. O'Hern, and B. Chakraborty, Entropy and Temperature of a Static Granular Assembly: An *ab initio* Approach, *Phys. Rev. Lett.* **99**, 038002 (2007).
- [25] D. S. Dean and A. Lefèvre, Possible Test of the Thermodynamic Approach to Granular Media, *Phys. Rev. Lett.* **90**, 198301 (2003).
- [26] The HiRISE Project, Online image: Polygonal patterned ground (2007), https://www.uahirise.org/PSP_002140_2025.
- [27] See Supplemental Material at <http://link.aps.org/supplemental/10.1103/PhysRevResearch.3.L042001> for supplemental results, data, and some details of the mathematical derivation which complements the main text.
- [28] Flying The Nest, Bolivia salt flats, Salar de Uyuni, worlds largest mirror, $t=493$ s, 2017, https://www.youtube.com/watch?v=V_RFDqrJC9U&t=493s.
- [29] S. Chatterjee, S. Mandal, and D. Banerjee, Variation of supergranule parameters with solar cycles: Results from century-long Kodaikanal digitized Ca II K data, *Astrophys. J.* **841**, 70 (2017).
- [30] R. A. Johnson and D. W. Wichern, *Applied Multivariate Statistical Analysis*, 6th ed. (Pearson Prentice Hall, London, UK, 2007), p. 76.
- [31] E. L. Lehmann, *Elements of Large-Sample Theory* (Springer, New York, NY, 1999).
- [32] M. E. Gurtin, E. Fried, and L. Anand, *The Mechanics and Thermodynamics of Continua* (Cambridge University Press, Cambridge, 2010).
- [33] R. Blumenfeld and S. F. Edwards, Granular Entropy: Explicit Calculations for Planar Assemblies, *Phys. Rev. Lett.* **90**, 114303 (2003).